Resistive Switching and Polarization Reversal of Hydrothermal-Method-Grown Undoped Zinc Oxide Nanorods by Using Scanning Probe Microscopy Techniques

Juanxiu Xiao,[†] Wei Li Ong,[‡] Ziming Guo,[∇] Ghim Wei Ho,[‡,∇] and Kaiyang Zeng*,[†]

[†]Department of Mechanical Engineering, National University of Singapore, 9 Engineering Drive 1, Singapore, 117576
[‡]Department of Electrical and Computer Engineering, National University of Singapore, 4 Engineering Drive 3, Singapore, 117576
[∇]Engineering Science Programme, National University of Singapore, 4 Engineering Drive 3, Singapore, 117576

S *Supporting Information*

ABSTRACT: This paper reports the localized electrical, polarization reversal, and piezoelectric properties of the individual hexagonal ZnO nanorods, which are grown via the hydrothermal method and textured with [0001] orientation. The studies are conducted with conductive atomic force microscopy (c-AFM) and piezoresponse force microscopy (PFM) techniques. The correlation between the resistance switching and polarization reversal is discussed. The c-AFM results show that there is less variation on the set or reset voltage in nanorod samples, compared to that of the ZnO thin film. With increasing aspect ratio of the nanorods, both set and reset voltages are decreased. The nanorods with low aspect ratio show unipolar resistance switching, whereas both unipolar and bipolar resistance switching are observed when the aspect ratio is larger than 0.26. The PFM results further show the ferroelectric-like property in the nanorods. Comparing with that of the ZnO thin film, the enhanced piezoresponse in the nanorods can be attributed to the size effect. In addition, the piezoresponse force spectroscopy (PFS) experiments are conducted in ambient air, synthetic air, and argon gas. It shows that the depolarization field in the nanorod may be due to the moisture in the environment; moreover, the increased piezoresponse may relate to the absence of oxygen in the environment. It is also shown that the piezoelectric responses increase nonlinearly with the aspect ratio of the nanorods. By comparing the piezoresponse hysteresis loops obtained from the nanorod samples of as-grown, air-annealed and vacuum-annealed, it is found that the oxygen vacancies are the origin of the polarization reversal in ZnO nanorods. Finally, the tradeoff between the electrical and ferroelectric-like properties is also observed.

KEYWORDS: *ZnO nanorods, resistance switching, polarization reversal, size effect, c-AFM, PFM*
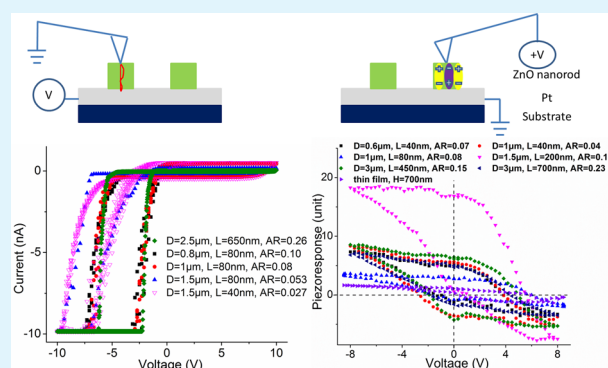
1. INTRODUCTION

Zinc oxide (ZnO) nanostructures have unique optical, electrical, piezoelectric, and ferroelectric-like properties. These structures have great potential for applications such as nano-optielectric, nanosensor, nanogenerator, nanostorage, and nanomemory devices.[1−7] Furthermore, the properties of the nanostructures can be enhanced by scaling down their dimensions.[8] The phenomena are most likely due to either the increases in the surface-to-volume ratio or the more unidirectional structures at the nanoscale. Recently, the resistive switching (RS) behavior has also been reported and extensively studied in undoped ZnO nanorods,[9−11] nanocolumns,[12] and nanoislands.[13] Compared to the thin film samples, one-dimensional (1D) ZnO nanostructure can reduce the variation of the set or reset voltage due to the localized vertical filaments in the unidirectional structure. Recently, Gupta and his colleagues reported the existence of enhanced ferroelectricity in V-doped ZnO nanorods at room temperature by using Sawyer−Tower hysteresis bridge, which paved the way for the application as ferroelectric random access memories (FeRAMs) at the nanoscale.[14] In their study, stronger polarity of V−O bonds was considered as the induction of the high value of polarization. Furthermore, Ghosh et al. also reported the ferroelectricity in undoped ZnO nanorods and proposed that zinc interstitial defects might be attributed to the existence of ferroelectricity.[15] In addition, the effects of size, surface tension, and depolarization field on ferroelectricity of the nanostructures with different shapes in ambient air were theoretically studied by Morozovska et al.[16] They have found that the ferroelectric properties in confined nanorods could be enhanced. The piezoelectric property of ZnO nanostructures is also intriguing to many studies with the purpose of applications such as nanoscaled sensors and generators. The size-independent piezoelectric properties of the solution-grown ZnO nanorod

were reported by Scrymgeour et al.[17] They have studied nanorods with lengths of 400−600 nm and diameters of 150−500 nm. In their study, however, the surface of the nanorod was etched by plasma, which might change the as-grown structures. Furthermore, AC voltage ranging of the 0 to 10 V may exceed the coercive bias and switched the piezoelectric domains in the as-grown nanorods.[17] Therefore, it is necessary and ideal to apply a piezoresponse force microscopy (PFM) technique to study the ferroelectric-like behavior in ZnO nanorods.[18,19] However, there are no experimental studies on the size effects and depolarization field on ferroelectric-like property of ZnO nanorod samples. Also, the correlations between the electrical and ferroelectric-like properties in ZnO nanorod samples have not been reported.

In this study, the size effects of the nanorod on electrical, piezoelectric, and ferroelectric-like properties are investigated. The resistive switching behavior is also correlated with the polarization reversal. In this work, the ZnO nanorods were grown via the hydrothermal method. Through appropriate strategies, this method can grow one-dimensional (1D) nanostructures at low temperature with simple and economic fabrication processes.[4,20] To minimize the lattice mismatch between the substrate and nanorods as well as to obtain the ZnO nanorods with [0001] textured, spinel substrate was used for the epitaxy growth.[21] During the sample preparation, a thin platinum layer was deposited on the spinel substrate and served as a conductive layer for the subsequent characterization by scanning probe microscope (SPM), measurements, this is because of the SPM tips used in this study are platinum-coated silicon tips. Hence, the Pt bottom electrode will induce the symmetric Schottky contact in Pt/undoped ZnO nanorod interfaces. In addition, for ZnO thin film, it was found that Pt as the bottom electrode gives rise to better polarization than those in samples with indium tin oxide (ITO) and Au bottom electrode, as the gold electrode may induce Ohm contact interface with the ZnO surface.[22−24] In addition, it is found this thin Pt layer does not play a role in promoting growth on the substrate; it does not hinder the growth of ZnO on the spinel substrate either.

PFM is a powerful technique to characterize the piezoelectricity and ferroelectricity in thin films structures; however, it is still a challenging issue when the PFM technique is applied to nanorods. First, it is difficult for the probe to be positioned precisely on the top of the nanorod if the diameter of nanorods is <100 nm, because of the thermal drift of the SPM system. Second, in the mapping mode of the SPM technique, the nanorods should not be too high, to avoid sharply increasing loading force and damaging the tip. To overcome these challenges, in this study, well-textured individual ZnO nanorods of large diameter (0.6−3 μm) and height (40−700 nm) were deposited and used. In addition, before the c-AFM and PFM measurements, the topography of the nanorods was first characterized using non-contact-mode AFM. Second, to avoid the damage of the SPM tips, the SPM scans were only localized to certain points or areas within the surface of the nanorods.

2. MATERIALS AND EXPERIMENTAL PROCEDURE

2.1. Sample Preparation. A spinel substrate was cleaned using deionized water (DI), followed by ethanol, for 5 min in each step. After drying with a stream of nitrogen (N_2) gas, 10 nm of platinum (Pt) layer was sputtered onto the substrate. To grow the ZnO nanorods, 12.5 mL of a growth solution was prepared by mixing zinc nitrate hexahydrate (ZN, $Zn(NO_3)_2 \cdot 6H_2O$, 0.04 M), hexamethylene-

tetramine (HMT, $C_6H_{12}N_4$, 0.0125 M) and ammonium nitrate (AN, NH_4NO_3, 0.15 M). The substrate was placed into the growth solution and heated at 90 °C for 50 min. The nanorod samples were then rinsed in ethanol and dried in air at 55 °C.

2.2. Characterization. *A. Topography and Crystal Structure.* Scanning electron microscopy (SEM) and atomic force microscopy (AFM) are used to characterize the topography and roughness of ZnO nanorods, respectively. The crystal orientation of the epitaxial growed ZnO narorods was determined by using X-ray diffraction (XRD) (Shimadzu, Model XRD-7000, Japan) with a monochromatic Cu Kα radiation source (λ = 0.1506 nm). The X-ray profiles were recorded in continuous θ−2θ scan mode with the 2θ angle between 30° and 65°. The scan speed was 0.5°/min. The operation voltage and current were 40 kV and 30 mA, respectively. The results confirmed that the nanorod samples are fully crystalline, with a [0001] orientation.

B. Photoluminescence (PL) Measurements. The photoluminescence (PL) was carried out at room temperature with He−Cd laser (Renishaw Raman and PL Microspectroscopy System 2000, Renishaw PLC, U.K.). The excitation wavelength is 325 nm.

C. c-AFM and PFM Studies. In this study, the commercial SPM system (MFP-3D, Asylum Research, USA), which was controlled by commercial software (IGOR PRO 6.34A and Asylum Research software, version 13.03.70), was used. In the c-AFM measurement, the effects of the set point (i.e., loading force) on local current−voltage (I−V) curves and current images were first studied. In the I−V curve measurements, a triangular voltage waveform with a frequency of 10 Hz and amplitude of ±10 V was used. The scan rate was 0.5 Hz. To obtain the current images, constant DC bias was applied to the bottom electrode (Pt). The schematic drawing of the c-AFM setup is shown in Figure S1(a) in the Supporting Information. To avoid the permanent electrical breakdown of the nanorods, a current compliance of 10 nA was preset. By analyzing these results, an optimized set point was found and then used in the subsequent c-AFM measurements.

In the PFM measurements, both lateral PFM and vertical PFM (the electric field is aligned orthogonal (lateral) or parallel (vertical) to the measured deformation), were conducted to obtain the images of topography, phase angle (φ), and amplitude (A). The amplitude image refers to the deflection of the cantilever caused by inverse piezoelectric effect. For the vertical PFM measurement, the out-of-plane deformation of the surface is registered through the deflection of the cantilever. The piezoelectric coefficient (d_{33}) can be obtained by using the formula

$$A_{\text{vertical}} = d_{33}E_{\text{ac}}$$

For the lateral PFM measurement, the electric-field-induced shear deformation of the sample surface causes torsional twist of the cantilever, and the piezoelectric coefficient (d_{15}) can be obtained using the formula

$$A_{\text{lateral}} = d_{15}E_{\text{ac}}$$

The phase image can yield the information on the polarization direction below the tip with regarding to the direction of the applied electric field. Phase angles equal to either 0° or 180° indicate that the polarization vector pointed either downward, toward the bottom electrode, or upward, toward the sample surface.

In the piezoresponse force spectroscopy (PFS) measurements (i.e., when the PFM was operated in the spectroscopy mode), the SPM tip was fixed at an arbitrary location and a triangle−square waveform with a frequency of 200 mHz was applied. The time for bias-on and bias-off was 25 ms, respectively. With the PFS technique, bias-on and bias-off phase hysteresis loops, $\varphi(E)$ and amplitude loops $A(E)$, can be obtained. The piezoelectric hysteresis loop, PR(E), is calculated from the equation

$$\text{PR}(E) = A(E) \cos[\varphi(E)]$$

In the calculation of PR(E), to exclude the electrostatic effect, both $\varphi(E)$ and $A(E)$ loops are obtained at the bias-off state. From the PR(E) hysteresis loops, several parameters can be extracted, including imprint bias (E_{im}), coercive bias (E_c), remanent switchable response

(R_0), maximum switchable response (R_s), and effective work of switching (A_s).

Imprint bias:

$$E_{im} = \frac{|V_p| - |V_n|}{2}$$

Coercive bias:

$$E_c = \frac{|V_p| + |V_n|}{2}$$

Remanent switchable response:

$$R_0 = R_0^+ - R_0^-$$

Maximum switchable response:

$$R_s = R_s^+ - R_s^-$$

Effective work of switching:

$$A_s = \int_{-\infty}^{+\infty} [R^+(V) - R^-(V)]\, d(V)$$

A schematic drawing of the PFM and PFS measurements is provided in Figure S1(b) in the Supporting Information). In this study, the PFS was conducted on the as-grown ZnO nanorods in ambient air, slow-flowing synthetic air, and argon gas, respectively. The synthetic air contains <5 ppm water, whereas the argon gas contains <0.02 ppm water and 0.01 ppm oxygen. The PFS was also conducted on the nanorods annealed in air (at atmospheric pressure) as well as in the vacuum (1×10^{-5} mbar), respectively; both are at 500 °C for 1 h.

The image resolution is dependent on the spatial resolution and the tip sharpness. To get good resolution, the SPM scan lines × points were kept as 256 × 256 pixels. The SPM tip should also be much sharper than the sample feature. The tip radius can be a few nanometers without coating. In the c-AFM and PFM measurements, the SPM tips are coated with a conductive coating, which would increase the tip radius. For this study, the commercial Pt-coated Si tips (Model AC240TM, Olympus, Japan) have an average tip radius of 15 nm and are relatively sharp. The tip has an average spring constant of 2 N/m, an average inverse optic lever sensitivity of 100 nm/V, and an average resonance frequency of 65 kHz. To protect the coating of the tip from wear and maximize the charge gradient across the domain boundaries, the scan angle was fixed at 90°, i.e., the scan orientation is normal to the length of the cantilever. The tip was continuously used in characterization of the $I-V$ properties of all the nanorods, and was only replaced when the uniform current images or repeatable $I-V$ curves cannot be obtained. Furthermore, to avoid the electrostatic effects during the PFM scan, the nanorods were grounded through the Pt bottom electrode. In these experiments, the relative humidity (RH) was ~60%.

3. RESULTS AND DISCUSSION

3.1. Topography and Crystal Structure. Figure 1a shows topography images obtained via SEM analysis. It clearly shows that the hexagonal ZnO nanorods nucleate and grow at random locations on the substrate. Generally speaking, the hexagonal unit cell of the nanorods consists of six nonpolar faces ($10\bar{1}0$), capped by either the polar O^{2-}-terminated ($000\bar{1}$) or Zn^{2+}-terminated (0001) basal planes.[25] The possible formation mechanism of nanorods may be layer-by-layer growth via an Ostwald ripening mechanism,[26] since multiple layered structures can be observed in the AFM image (Figure 1b). In the formation process, zinc nitrate provides the Zn^{2+} ions while HMT provides OH^- ions and serves as a kinetic buffer of solution pH.[27] Those ions are combined to form ZnO via the reaction steps stated below:
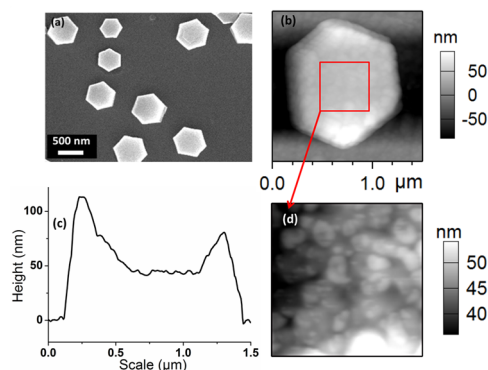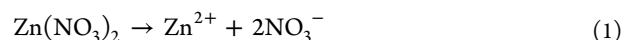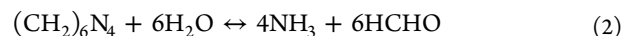

Figure 1. Topography images obtained by (a) SEM and (b) AFM. (c) Line profile of the AFM topography image shown in panel b. (d) Topography image of the central 0.5 μm × 0.5 μm area in the nanorod shown in panel b.

$$Zn(NO_3)_2 \rightarrow Zn^{2+} + 2NO_3^- \tag{1}$$

When the growth solution is heated, HMT hydrolyzes in water and gradually produces formaldehyde (HCHO) and ammonia (NH_3):

$$(CH_2)_6N_4 + 6H_2O \leftrightarrow 4NH_3 + 6HCHO \tag{2}$$

The ammonia then decomposes in solution to form OH^- ions:

$$NH_3 + H_2O \rightarrow NH_3 \cdot H_2O \tag{3}$$

$$NH_3 \cdot H_2O \leftrightarrow NH_4^+ + OH^- \tag{4}$$

The Zn^{2+} ions from the dissociated zinc nitrate solution then react with the OH^- ions to form $Zn(OH)_2$, which undergo a condensation reaction to form a water molecule and solid ZnO:

$$Zn^{2+} + 2OH^- \leftrightarrow Zn(OH)_2 \tag{5}$$

$$Zn(OH)_2 \rightarrow ZnO + H_2O \tag{6}$$

To obtain the nanorods with a low aspect ratio, ammonium nitrate is added to the growth solution to maintain the growth solution at a low pH value. According to the work by Richardson et al.,[28,29] a growth solution with a low pH value produces low-aspect-ratio ZnO nanorods while a high pH produces high-aspect-ratio ZnO nanorods. When ammonium nitrate is added, the presence of NH_4^+ ions from its dissociation (eq 7) slow the reversible reaction in eq 4, which reduces the concentration of the OH^- ions and results in a low pH value in the growth solution. As a result, ZnO nanorods with low aspect ratio will be formed.

$$NH_4NO_3 \rightarrow NH_4^+ + NO_3^- \tag{7}$$
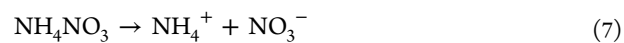
The surface roughness (i.e., the root-mean-square, RMS) is measured to be ~44.2 nm in the central area of 0.5 μm × 0.5 μm (see Figure 1d). It is obvious that the nanorod surface is relatively smooth without visible defects, such as holes, cracks, and protrusions. By analyzing the line profile on the AFM topography image (Figure 1b), the diameter, length, and aspect ratio of the nanorod are obtained (Figure 1c). In this study, the length of the nanorods ranges between 40 nm and 700 nm and diameters ranging between 600 nm and 3 μm are obtained using the method described above. In addition, XRD measurement has been conducted (see Figure S2 in the Supporting Information). Only a single peak is observed at 2θ = 34°. This peak is indexed as the (002) plane of the ZnO

hexagonal wurtzite structure, which is equivalent to the [0001] orientation. The single peak XRD pattern indicates that the ZnO narorods have a single crystal structure and are all textured in the [0001] orientation.

3.2. Photoluminescence (PL) Measurements. The photoluminescence (PL) measurements can validate the existence of oxygen vacancies in the ZnO nanorod samples. These measurements were conducted on as-grown ZnO nanorods as well as the nanorod samples that were annealed in air and under vacuum (1×10^{-5} mbar) at 500 °C for 1 h, respectively. The PL measurement results are shown in Figure S3 in the Supporting Information). It can be clearly seen that all of the samples have an ultraviolet emission at 380 nm, corresponding to the near-band edge emission of the ZnO.[30] However, the as-grown ZnO has a broad visible emission peak that is attributed to oxygen vacancies.[31] After annealing in air, the visible emission peak (at ~490−550 nm) disappears, which can be attributed to the combination of the oxygen vacancies of the ZnO nanorods with oxygen ions from the air.[32] Inversely, for the nanorods annealed under vacuum, the emission peak (at ~490−550 nm) is increased, because of the intentionally created oxygen vacancies under vacuum conditions.[33]

3.3. The Resistance Switching Studied by c-AFM. The electrical characterization of the individual [0001] textured ZnO nanorods is conducted on the top surface using the c-AFM technique. To avoid artificial effects due to the poor contact between the tip and the sample, the loading force of 40−200 nN (i.e., a setpoint of 0.4−2 V) is used when recording the local current−voltage (I−V) curves at certain locations (see Figure 2a). It shows unipolar resistance switching for the nanorods with a diameter of 1 μm and a length of 80 nm; the set voltage is −3 V, and the reset voltage is −7 V. There are almost no variation in the I−V curves as the loading force increased, which indicates that the loading force or voltage (setpoints) used has little effect on the I−V curves. Figures 2b and 2c are the current images obtained with the voltage (setpoint) of 0.2 and 0.8 V, respectively. The sample voltage for c-AFM scanning is 5 V. It is clear that the current image obtained with a setpoint of 0.8 V is clearer and less affected by the 90° scan angle. It is interesting to note that there are no current bursts inside the nanorod, i.e., the current value inside the nanorod is negligible, compared to that of the bottom electrode, except for some current spikes (shown in yellow) at the edges of the nanorod. If overlaying the current image on top of the topography image, it is obvious that the current spikes appear at the edges and sidewall of the nanorod, where there are large changes in height (Figure 2d). Hence, the current spikes may be due to the large changes of the loading force as the height of the nanorod changes abruptly. On the other hand, it was also reported that, for thin films with higher surface roughness because of the larger grain size, there might be more oxygen vacancies in the grain-boundary region, thus also reducing the resistivity in this region.[24] However, the current experiments cannot distinguish if there are more oxygen vacancies at the edge of the nanorods. Therefore, more research works are needed in the future to confirm this point.

To ensure good contact between the tip and the nanorod surface, as well as to avoid wear of the tip coating, and to achieve reproducible results, the setpoint is kept at 0.8 V in the subsequent c-AFM measurements, and the scan rate is 0.5 Hz. Furthermore, when the sample bias is increased to 10 V with a step increment of 1 V, there is still no current burst inside the nanorod (see Figure 2e). Note that there are also some current
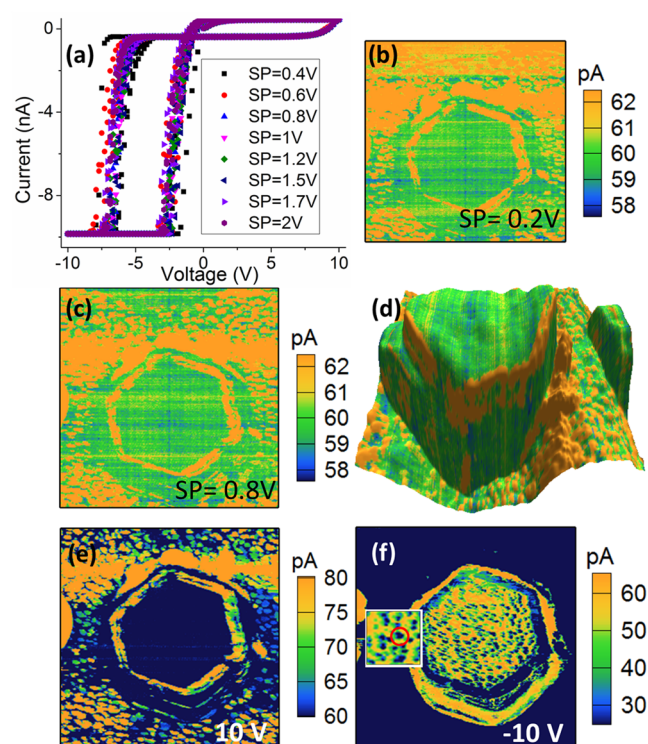

Figure 2. (a) Local current−voltage (I−V) curves with various loading forces between 40 nN to 200 nN, i.e., the c-AFM set-point of 0.4 to 2 V. (b) and (c) The current images scanned with set-point of 0.2 and 0.8 V respectively. (d) The current image is overlaid on topography image. Also shown are current images scanned with a sample bias of (e) 10 V and (f) −10 V. The inset in panel f shows an enlarged view of the current image. The current image size is 1.5 μm × 1.5 μm.

spikes appearing at the edges of the nanorod. However, when the sample bias decreases to −10 V, there are some current spikes occurring inside the nanorod (Figure 2f). These phenomena are consistent with the unipolar I−V curves observed (Figure 2a), which may be obtained at the locations where current spikes occurred. The current spikes can be seen more clearly from the inset of Figure 2f and marked with a red circle. In addition, the nanorod is at a high resistance state (HRS) under a positive sample biased region and can be switched into a low resistance state (LRS) by certain negative sample bias. The appearance of the unipolar switching behavior can be attributed to native defects, such as oxygen vacancy.[34,35] In the LRS, there is the formation of the conduction filaments and it is dominated by Ohmic conduction mechanism, whereas in the HRS, the conduction filaments are ruptured and the Schottky interface/Poole−Frenkel (PF) conduction mechanism dominates.[10,36]

The effects of the aspect ratio on the I−V curves of the nanorods are studied in order to determine the size effects on the resistive switching behavior of the nanorods. It is found that the variation of the set or reset voltage within one individual nanorod is below 0.5 V. The narrow dispersion of the set or reset voltage may be due to the vertically branched conductive filaments in the nanorods, as schematically shown in Figure 3a. Figure 3b is the I−V curves for the nanorods with aspect ratios ranging from 0.027 to 0.26. It is clear that, when the aspect ratio is >0.08, although the length varies from 80 nm to 650 nm and the diameter varies from 0.8 μm to 2.5 μm, there are only small changes in the set or reset voltage. It is also noticed that
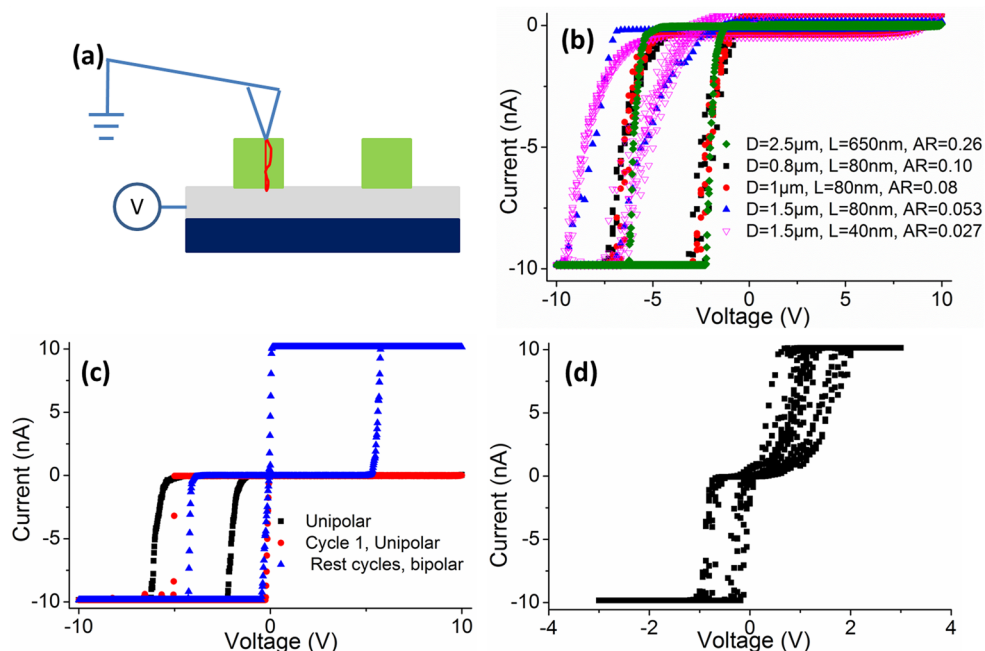
Figure 3. (a) Schematically diagram of the vertically branched conductive filaments in the nanorods. (b) $I-V$ curves for individual nanorods with length × diameter ($L \times D$) dimensions of 40 nm × 1.5 μm, 80 nm × 0.8 μm, 80 nm × 1 μm, 80 nm × 1.5 μm, and 650 nm × 2.5 μm, respectively. The aspect ratio (AR) ranges from 0.027 to 0.26 for those nanorods. (c) The coexisting of the unipolar and bipolar resistive switching in the nanorod with a diameter of 2.5 μm and a length of 650 nm. (d) $I-V$ curves for the ZnO thin film with a thickness of 40 nm.

the unipolar and bipolar resistive switching behaviors coexist in the nanorods with a diameter of 2.5 μm and a length of 650 nm (see Figure 3c). In certain locations, the bipolar resistive switching occurs after the first cycle of unipolar resistive switching (Figure 3c). The coexistence of both phenomena was also reported in ZnO films,[37] and it was found that the transition between these two switching modes could be controlled by the value of the compliance current in the electroforming process.[37] In addition, it is also found that both the set and reset voltages (absolute value) increase significantly with decreasing aspect ratio (ranging from 0.26 to 0.027). For comparison, a ZnO thin film with the same thickness as the length of the nanorods is also studied to determine whether there is effect due to the scaling down of the dimension. Figure 3d shows the $I-V$ curves for a thin film with a thickness of 40 nm. The bipolar resistive switching behavior is observed, even though the set voltage has a large variation due to the multidirectional bundled conductive filaments in the ZnO thin film.[10]

3.4. The Polarization Reversal Studied by PFM. Figures 4a−e show the respective topography, V-PFM, L-PFM amplitude, and phase images of the ZnO nanorod with a diameter of 1 μm and a length of 40 nm. The V-PFM phase image and its histogram (Figures 4d−g) show that almost all of the domains have a phase angle of −20°; this indicates that the spontaneous polarizations are along the c-axis orientation (i.e., [0001] orientation). On the other hand, some small patches with converse color contrast (yellow and purple colors) are observed in the L-PFM phase image (Figure 4e). These patches can be identified as domains with approximately opposite polarizations, which are also illustrated by the histogram of the phase images (Figure 4g). The phase angle difference is ∼160° (the phase angle for the domains shown in purple is approximately −150° and the phase angle for the domains shown in yellow is ∼10°). The domains' orientations are

further verified by line profiling, as shown in Figure 4f. Since the amplitude image is proportional to the magnitude of the piezoelectric coefficient (d_{33}), the piezoresponse at the domain walls is obviously lower than that in the internal of the domains.[38] It is worth mentioning that there is almost no apparent change in the V-PFM amplitude image (Figure 4b), whereas an abrupt change at the domain wall region can be observed in the L-PFM amplitude image (Figure 4c).

Furthermore, the domain switching by DC poling processes of the as-grown ZnO nanorod is studied. Figures 5a and 5b show V-PFM phase and amplitude images after the poling processes with the tip bias of 10 V tip on the area marked by red and −10 V (tip bias) on the area marked by green, respectively. It can be seen that the domains in the as-grown nanorod is in the upward direction (yellow color), but after poling with 10 V tip bias, the upward domain is switched to downward direction (purple color). On the other hand, when poling with −10 V tip bias, the domains remain in the upward direction.

These domain switching processes by poling further confirm the ferroelectric-like property of the ZnO nanorods. The domain switching is also clearly shown in Figure 5f (i.e., the line profile of the V-PFM phase image in Figure 5a), and the result suggests that the domain switching with a phase angle change of ∼180° is achieved by these poling processes. Figures 5d and 5e show the corresponding lateral PFM phase and amplitude images, which also show certain in-plane domain switching processes when poling with a tip bias of 10 V. It is worth noting that the difficulty in switching the polarization to a downward direction, using a tip bias of 10 V (or a sample bias of −10 V) may be related to the electrical property of the nanorod. Certain locations in the nanorod poled with a sample bias of −10 V are under LRS (Figure 2f), and this will hinder the ferroelectric-like property in the nanorods.[39] It is also interesting to note that the poling processes can affect the
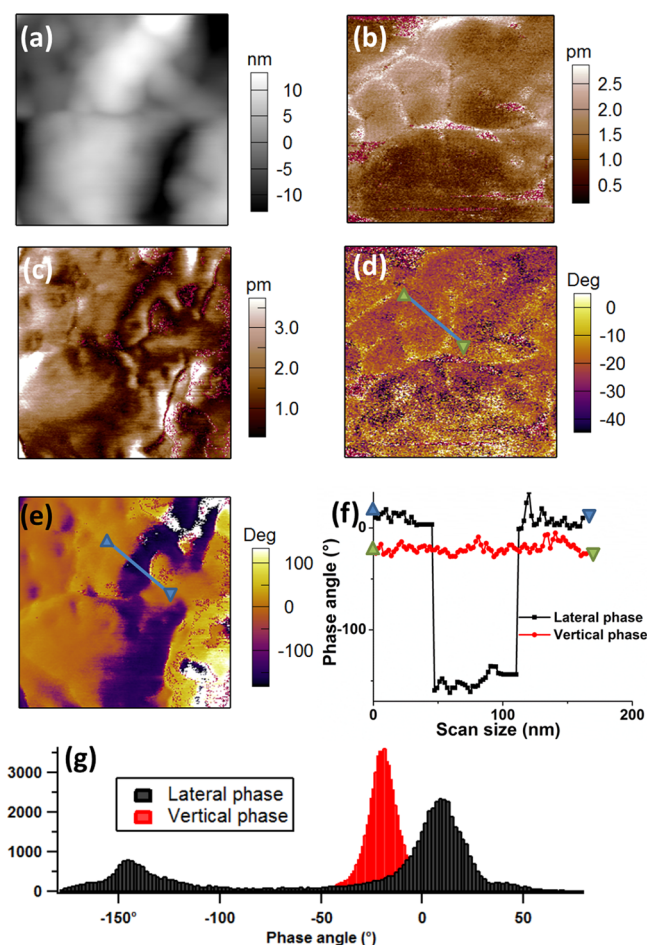
Figure 4. (a) Topography, (b) V-PFM, (c) L-PFM, (d) amplitude, and (e) phase images of the ZnO nanorod 1 μm in diameter and 40 nm in length. (f) Line profiles of the phase images shown in panels d and e. (g) Histogram of the phase images shown in panels d and e. The size for the phase and amplitude images is 0.5 μm × 0.5 μm.
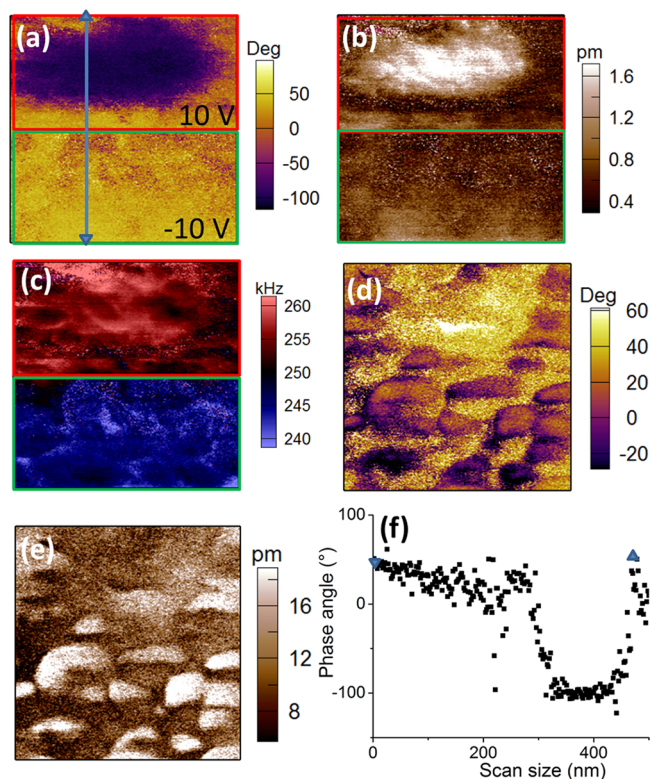
Figure 5. V-PFM (a) phase and (b) amplitude images after poling processes with the application of 10 V on the area marked by red and −10 V on the area marked by green, respectively. (c) Resonant frequency image after the poling processes with tip biases of 10 V and −10 V. Also shown are the corresponding lateral PFM (d) phase and (e) amplitude images, and (f) the line profile of the V-PFM phase image. The size for the phase and amplitude images is 0.5 μm × 0.5 μm.

resonant frequency image (Figure 5c). The resonant frequency is associated with the contact stiffness and represents the information on the local elastic properties.[40] Hence, this result suggests that poling may also affect the elastic properties of the nanorods. The ferroelectric-like behavior in ZnO nanorods under room temperature is further verified by the PFS technique in the next section.

3.5. The Polarization Reversal Studied by PFS. Following the preliminary PFM study, the ferroelectric-like behavior is further verified using the PFS measurements. In the PFS study, the AC voltage is kept constant at 1.2 V. Figures 6a and 6b show the "butterfly"-shaped amplitude loop ($A(E)$) and hysteresis loop in phase angle [$\varphi(E)$], with a window bias of ±8 V, respectively. The phase angle loop shows a 180° difference, and this indicates that the polarizations can be switched to upward or downward direction by the external electric field. This also confirms the ferroelectric-like behavior in the ZnO nanorod. In addition, the positive and negative coercive voltages can be deduced from the PR(E) loop when the piezoresponse is zero. The piezoresponse hysteresis loop, PR(E), can be calculated and plotted using the equation[18]

$$PR(E) = A(E) \cos[\varphi(E)]$$

To investigate the effects of the DC voltage on the saturated piezoresponse hysteresis loop for the ZnO nanorods, the DC voltages are varied from ±4 V to ±12 V. The representative piezoresponse hysteresis loops are shown in Figure 6c. The PR(E) hysteresis loops are clearly dependent on the DC voltage, and the effective work of switching (area enclosed by the PR(E) loop) increases with the increased DC voltage. However, the PR(E) hysteresis loops are asymmetric; this may be due to the screen charge from the leakage current. The high conductivity of the nanorods may be due to the intrinsic defects, such as oxygen vacancies, which was verified in the previous PL measurements. In addition, the shift along the electric field axis to the positive bias suggests that there is a built-in field, which favors the original polarization in the [0001] orientation.[41,42] The loops are also shifted along the vertical axes; this suggests that the piezoresponse of the film is more sensitive to the negative bias than that to the positive bias. This may be related to the frozen layer and incomplete back switching in the thin film, as reported previously.[42] This existence of ferroelectric-like behavior and the evolution of PR(E) hysteresis loops with DC voltage are also investigated on the nanorod with a diameter of 0.6 μm and a height of 40 nm (see Figure S4 in the Supporting Information).

To clarify whether there is correlation between the domain states and PR(E) hysteresis loops, the PFS measurements are conducted in the unbiased region and the regions after the DC poling processes (poled with 10 V/−10 V) on the same as-
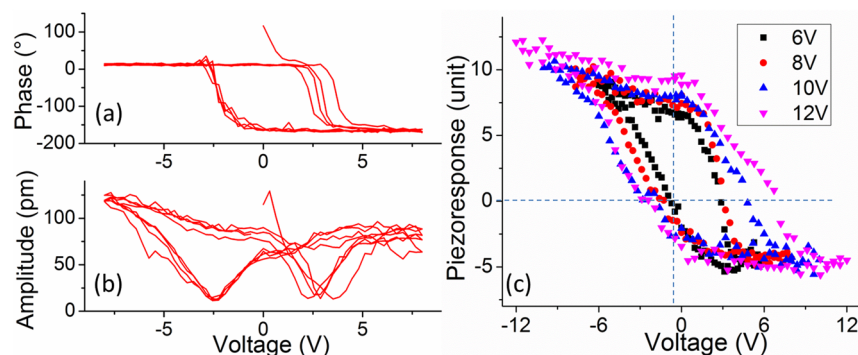
Figure 6. (a) Amplitude "butterfly" loop ($A(E)$) and (b) phase hysteresis loop ($\varphi(E)$) obtained with a DC voltage of 8 V. (c) The piezoresponse hysteresis loop, $PR(E)$, which is calculated and plotted using the equation $PR(E) = A(E) \cos[\varphi(E)]$.
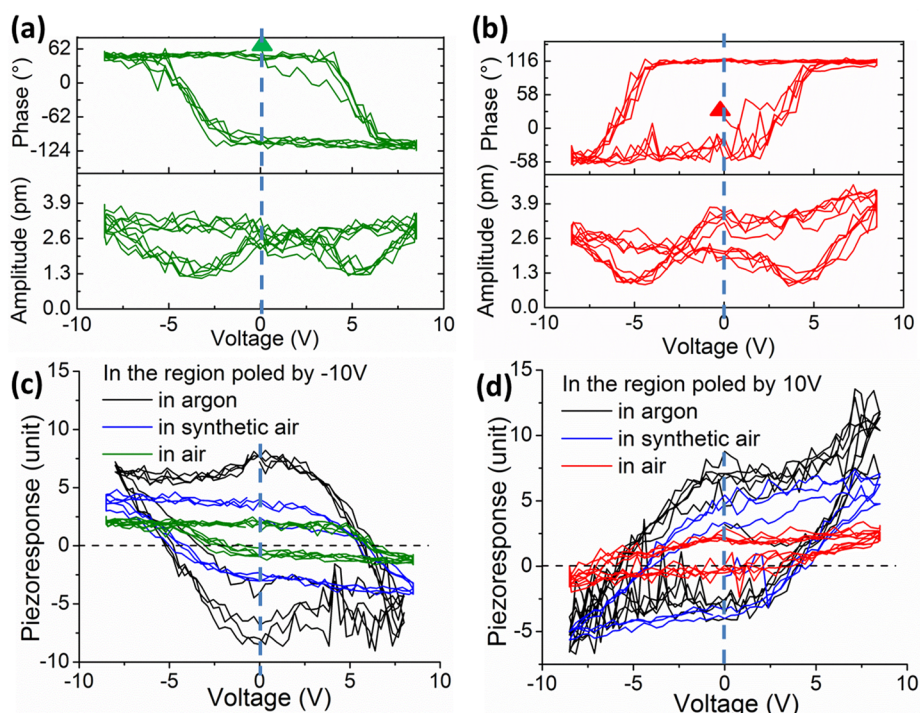

Figure 7. (a) Phase hysteresis loops and (b) butterfly-like amplitude loops obtained in the regions poled with −10 V and 10 V. Also shown are $PR(E)$ hysteresis loops obtained in both regions ((c) in the region poled by −10 V and (d) in the region poled by 10 V) via the same PFS technique conducted in different environments.

grown nanorod. It is found that the saturated phase hysteresis loops and butterfly-like amplitude loops can be obtained in all regions (see Figures 7a and 7b). The calculated $PR(E)$ hysteresis loops of different regions are plotted in Figures 7c and 7d. The $PR(E)$ hysteresis loops obtained in the unbiased region are similar to those obtained in the region poled with −10 V (see Figure 7c). However, the $PR(E)$ hysteresis loops obtained in the region poled with 10 V are different (see Figure 7d). The hysteresis loops in the unbiased region or the region poled with −10 V oriented different from the region poled with 10 V along the applied electric field direction, and this is most likely due to the different initial states of the domains, which may initiate different polarization switching processes (marked in Figures 7a and 7b). In the unbiased region and the region poled with −10 V, the polarization orientation is upward and contributes to a positive built-in field, which favors the polarization in the [0001] orientation. In contrast, in the region poled with 10 V, the polarization is downward and may

account for the existence of a negative built-in field; and this favors the polarization in the [000$\bar{1}$] orientation. Furthermore, in the unbiased region and the region poled with −10 V, the hysteresis loops are apparently in an "anti-poling" shape, i.e., they are oriented in the opposite direction of the applied field. It shows that the shape of the piezoresponse hysteresis loop ($PR(E)$) relates to the shape of phase hysteresis loops [$\varphi(E)$], in which is decided by the initial phase angle.

To further confirm whether the ferroelectric-like behavior is the intrinsic behavior of the nanorods, and to also to rule out the effects of moisture and oxygen from the ambient condition, the PFS measurements are further conducted under synthetic air and argon gas in the regions poled by 10 V or −10 V, respectively. The results are similar to those obtained under ambient conditions and therefore confirmed that the ferroelectric-like property is the intrinsic property of the ZnO nanorods (Figures 7c and 7d). It should be noticed that the built-in field is slightly reduced in either synthetic air or argon
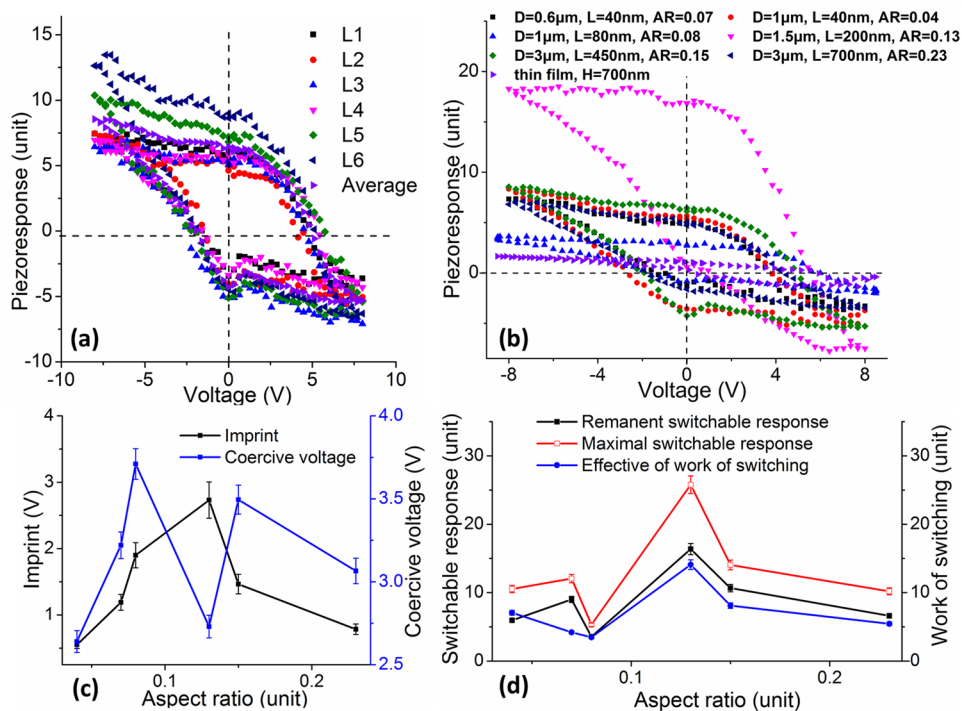
Figure 8. (a) PR(E) hysteresis loops obtained at six different locations of the nanorod with a diameter of 1 μm and a length of 40 nm and the averaged PR(E) hysteresis loop of these hysteresis loops obtained from varied locations. (b) All of the averaged PR hysteresis loops from varied nanorods and thin film. [In the legend, D is the diameter, L is the length, and AR is the aspect ratio.] (c, d) Imprint bias (E_{im}), coercive bias (E_c), remanent switchable responses (R_0), maximum switchable responses (R_s), and the effective work of switching (A_s), plotted as a function of aspect ratio of the nanorods. The error bars in panels c and d are ~5%.

gas. The decreased built-in field in synthetic air and argon gas may be due to the absence of moisture in these two environments. In the ambient condition, the moisture can cause the effects of the screen charges.[18] In addition, there are increased values of the forward and reverse saturation and remnant piezoresponses in either synthetic air or argon gas, and the increments in argon gas are larger than those in the synthetic air. This suggests that the absence of oxygen in the argon environment may account for the increased piezoresponse.

To correlate the ferroelectric-like properties and nanorod's geometric dimension, the PFS measurements are further conducted at six random locations of one rod. Furthermore, those experiments are conducted on the rods with the same aspect ratio, as well as on rods with different aspect ratios (ranging from 0.04 to 0.23, i.e., different diameters (ranging from 0.6 μm to 3 μm) and length (ranging from 40 nm to 700 nm)). In addition, the PR(E) hysteresis loop of the ZnO thin film with a thickness of 700 nm deposited via the same chemical method is also studied. The PR(E) hysteresis loops are calculated based on the amplitude and phase loops as described previously. Figure 8a shows the PR(E) hysteresis loops and the average PR(E) hysteresis loop (obtained at six different locations) from the nanorod with a diameter of 1 μm and a length of 40 nm. It shows relatively small scatter with the locations in one nanorod. All of the averaged PR(E) hysteresis loops obtained from various nanorods and thin film are plotted in Figure 8b. It clearly reveals that the ferroelectric-like behavior of the nanorods is significantly enhanced, compared to that of the thin film. The hysteresis loop for thin film is narrow and with very small values of R_0, R_s, and A_s, but large E_{im} and E_c.

The hysteresis loops of the nanorods show high values of R_0, R_s, and A_s, but low values of E_{im} and E_c. The enhanced ferroelectric-like behavior may be due to the size effect. In the nanorod, the dipole moment per unit volume is significantly increased.[16,43] One of the possible reasons is the radial pressure caused by the surface tension in nanorods.[8,16] The results also highlight that the ZnO nanorod has potential applications for nanoscale nonvolatile ferroelectric memory devices. Figures 8c and 8d show the PR(E) parameters as a function of the aspect ratio of the nanorod. When the aspect ratio is within a range of 0.04−0.23, the values of E_{im}, E_c, R_0, R_s, and A_s first increase and then decrease, with the largest E_{im}, R_0, R_s and A_s values but relatively smaller E_c value being observed for the nanorod with an aspect ratio of 0.13. The nanorod with an aspect ratio of 0.07 has the largest E_c value and a relatively larger E_{im} value, it also has the smallest values of R_0, R_s, and A_s. Conventionally, since the imprint may not only come from the inherent property of the nanorod, but also by charge injections, the nanorod with an aspect ratio of 0.13 shows better ferroelectric-like properties, whereas the nanorod with an aspect ratio of 0.07 shows poor ferroelectric-like properties. In addition, the c-AFM and PFM results show that increasing the aspect ratio can reduce the set and reset voltages; however, the ferroelectric-like property does not increase linearly with the aspect ratio.

Generally speaking, two factors may contribute to the ferroelectric-like property in the pure ZnO-based materials. One factor is that the oxygen vacancy in the nanorods may assist the polarization switching processes, in which the domain reversal occurs at the vicinity of the oxygen vacancy. The oxygen vacancy can also lower the activation energy and assist the accomplishment of the domain movement.[44] The other factor is that the large lattice mismatch between the substrate

and nanorods due to the zinc interstitial defects might be attributed to the existence of ferroelectric-like property.[15] In this study, a ferroelectric-like property study is conducted on the nanorods with the same diameter but different length. If the lattice mismatch between the substrate and nanorods lead to the occurrence of ferroelectric-like property, the rods should show the same ferroelectric-like property. However, the results show that the nanorods with a diameter of 1 μm and a length of 40 nm have better ferroelectric-like property than that in the nanorod with a diameter of 1 μm and a length of 80 nm. Hence, the oxygen vacancy in the nanorods is most likely the reason for the ferroelectric-like property. This hypothesis is also confirmed by comparing the ferroelectric-like property of the nanorods (3 μm in diameter) with lengths of 450 and 700 nm. The hypothesis of oxygen-vacancy-assisted polarization reversal was further verified by conducting the PFS measurements on the nanorods under air annealing and vacuum annealing. (See Figures S5(d)−(g) in the Supporting Information.) For the nanorods annealed in air, it is obvious that there are no changes in the phase angle but there is still some deformation of the surface originated from the converse piezoresponse effect (Figures S5(d) and S5(e) in the Supporting Information). This can be due to the reducing oxygen vacancies in the nanorods by air annealing (see Figure S3 in the Supporting Information). On the other hand, for the nanorods annealed under vacuum conditions, the "butterfly"-shaped amplitude loops and saturated phase loops (Figures S5(f) and S5(g) in the Supporting Information) show that the magnitude of the amplitude is increased, in comparison to that of the as-grown nanorod samples (shown in Figures 7a and 7b). This increased ferroelectric-like property can result from the increased number of oxygen vacancies in the vacuum-annealed nanorods (see Figure S3 in the Supporting Information). On the other hand, it should mentioned that, in this study, the polarization reversal in the as-grown ZnO nanorods is not induced by the hydrogen interstitial defects.[45,46] Hydrogen interstitial defects could be strong in the as-grown ZnO nanorods, because the synthesis is via a hydrothermal method.[47] Nevertheless, hydrogen impurity bonding with an oxygen atom can form a H−O dipole, which may increase the bulk ferroelectric polarization in some ferroelectric materials such as $BaTiO_3$ and $PbTiO_3$.[48,49] On the other hand, the formation of H−O can also lead to the loss of oxygen ions and reduce the switching charges. It was also observed that the polarization hysteresis in these materials disappeared because of the reduction in the switching charges.[48,49] The ferroelectric-like property can be restored after annealing the sample in air,[48,49] since the hydrogen interstitials can be removed during the annealing. However, in this study, the ferroelectric-like property is degraded in the air-annealed nanorods. This suggests that the reduction of the oxygen vacancy makes the polarization reversal difficult. In addition, the tradeoff between the electrical property and ferroelectric-like property is also observed in the air-annealed ZnO nanorods. It is found that the air-annealed nanorods, which have poor ferroelectric-like properties, are more conductive. This enhanced conductivity can be explained by the oxygen surface passivation effect and an enhanced crystallite structure.[47] Figure S3 in the Supporting Information shows that the oxygen vacancy is reduced in ZnO nanorods after air annealing, which may cause the oxygen surface passivation effect and decrease the number of oxygen defects. This can reduce the surface barrier; hence, the carrier mobility and conductivity can be increased. On the other hand, it was

reported that ZnO annealed in air at higher temperature up to 600 °C can result in a decrease in resistivity, in terms of enhancement of the crystallite structure.[50,51] In this study, the absolute set and reset voltage can be <1 V (see Figures S5(a)−(c) in the Supporting Information).

3.6. The Piezoelectric Property Studied PFM. The PFS results suggest that the AC voltage in the piezoelectricity study should be below 4 V for nanorods. The piezoresponse, $A(E)$, i.e., the bias-induced deformation along the [0001] orientation, can be calculated by multiplying the piezoelectric coefficient, d_{33}, with the applied electric field, E_{ac}. Therefore, the piezoelectric coefficient, d_{33}, can be calculated from the V-PFM measurements. In this study, the piezoelectric coefficients (d_{33}) of the individual nanorods are found within the range of 1−3 pm/V. This is smaller than what was reported by Scrymgeour et al.[17] This may be due to the nanorods used in this work having smaller aspect ratios. These results also suggest that the piezoelectric coefficients may not have a simple dependence on the physical dimensions of the nanorods, such as the diameter and length. Furthermore, the piezoelectric coefficient (d_{15}) is also determined from the L-PFM measurement and the results show that the value of d_{15} varied from 2.2 pm/V to 7.6 pm/V.

4. SUMMARY AND CONCLUSIONS

In this study, individual hexagonal nanorods with relatively low aspect ratios (0.04−0.26) are grown via the hydrothermal method. The topography of the ZnO nanorod is characterized by using scanning electron microscopy (SEM) and atomic force microscopy (AFM). The XRD results also confirm that the nanorods have a textured [0001] orientation. The electrical properties of the individual nanorods are studied by using the conductive atomic force microscopy (c-AFM) technique. The characteristics of the current−voltage ($I−V$) curves show unipolar resistance switching; the set or reset voltage decreases as the aspect ratio of the nanorods increases. However, when the aspect ratio increases to 0.26, the nanorods show both unipolar and bipolar resistance switching characteristics. The narrow dispersion of the set or reset voltage for nanorods, in contrast to that of a thin film, may be due to the vertically localized conductive filaments. The ferroelectric-like properties of the nanorods are then studied. The domain structure is first characterized by vertical and lateral piezoresponse force microscopy (PFM) techniques. The results have confirmed that the nanorods show the ferroelectric-like behavior. This behavior can be well-explained by the oxygen-vacancy-associated domain switching under the biased tip. Furthermore, the size effect on the ferroeletric-like properties has also been studied. Despite the smallest coercive bias (E_c) being observed in the nanorod with an aspect ratio of 0.13, the results show that the imprint bias (E_{im}), remanent switchable response (R_0), maximum switchable response (R_s), and effective work of switching (A_s) values first increase and then decrease with increasing aspect ratio, over an aspect ratio range from 0.04 to 0.23. However, the PFM results do not suggest any correlation between the piezoelectric coefficients and the physical dimensions of the nanorods. The observed abnormal hysteresis loops are partially caused by the surface being screened from the humidity (moisture in the air) conditions. This is proven by the PFS results obtained in synthetic air and argon gas. However, there is still a small drift along the voltage axis, which may be due to the dead layer and intrinsic defects in the nanorods. Therefore, more studies are needed to have a better

understanding of these phenomena. To conclude, the results also highlight the potential applications of the ZnO nanorod in nanoscale nonvolatile resistive or ferroelectric memory devices.

■ ASSOCIATED CONTENT

ⓢ Supporting Information

Schematic drawings of the c-AFM setup and the PFM/PFS setup. XRD intensity as a function of the angle 2θ for ZnO nanorods. The PL spectra of the ZnO nanorods samples under as-grown and air- and vacuum-annealed conditions. PR(E) hysteresis loops with varied DC voltage for the nanorod with a diameter of 0.6 μm and a length of 40 nm. The current images and $I-V$ curves, as well as PFS results for annealed nanorods with diameters of 1 μm and lengths of 40 nm. The Supporting Information is available free of charge on the ACS Publications website at DOI: 10.1021/acsami.5b01988.

■ AUTHOR INFORMATION

Corresponding Author
*Tel.: +65-6516-6627. Fax: +65-6779-1459. E-mail: mpezk@ nus.edu.sg.

Notes
The authors declare no competing financial interest.

■ REFERENCES

(1) Joseph, M.; Tabata, H.; Kawai, T. Ferroelectric Behavior of Li-Doped ZnO Thin Films on Si(100) by Pulsed Laser Deposition. *Appl. Phys. Lett.* **1999**, 74 (17), 2534−2536.

(2) Özgür, Ü.; Alivov, Y. I.; Liu, C.; Teke, A.; Reshchikov, M.; Doğan, S.; Avrutin, V.; Cho, S.-J.; Morkoc, H. A Comprehensive Review of ZnO Materials and Devices. *J. Appl. Phys.* **2005**, 98 (4), 041301.

(3) Yao, I. C.; Lee, D. Y.; Tseng, T. Y.; Lin, P. Fabrication and Resistive Switching Characteristics of High Compact Ga-Doped ZnO Nanorod Thin Film Devices. *Nanotechnology* **2012**, 23 (14), 145201.

(4) Yi, G.-C.; Wang, C.; Park, W. I. ZnO Nanorods: Synthesis, Characterization and Applications. *Semicond. Sci. Technol.* **2005**, 20 (4), S22−S34.

(5) Espinosa, H. D.; Bernal, R. A.; Minary-Jolandan, M. A Review of Mechanical and Electromechanical Properties of Piezoelectric Nanowires. *Adv. Mater.* **2012**, 24 (34), 4656−4675.

(6) Wang, Z. L.; Song, J. Piezoelectric Nanogenerators Based on Zinc Oxide Nanowire Arrays. *Science* **2006**, 312 (5771), 242−246.

(7) Wagner, A.; Bakin, A.; Otto, T.; Zimmermann, M.; Jahn, B.; Waag, A. Fabrication and Characterization of Nanoporous Zno Layers for Sensing Applications. *Thin Solid Films* **2012**, 520 (14), 4662−4665.

(8) Gupta, M. K.; Kumar, B. Enhanced Ferroelectric, Dielectric and Optical Behavior in Li-Doped ZnO Nanorods. *J. Alloys Compd.* **2011**, 509 (23), L208−L212.

(9) Beinik, I.; Kratzer, M.; Wachauer, A.; Wang, L.; Lechner, R. T.; Teichert, C.; Motz, C.; Anwand, W.; Brauer, G.; Chen, X. Y.; Hsu, X. Y.; Djurišić, A. B. Electrical Properties of ZnO Nanorods Studied by Conductive Atomic Force Microscopy. *J. Appl. Phys.* **2011**, 110 (5), 052005.

(10) Chang, W.-Y.; Lin, C.-A.; He, J.-H.; Wu, T.-B. Resistive Switching Behaviors of ZnO Nanorod Layers. *Appl. Phys. Lett.* **2010**, 96 (24), 242109.

(11) Park, S.; Lee, J. H.; Kim, H.-D.; Hong, S. M.; An, H.-M.; Kim, T. G. Resistive Switching Characteristics of Sol−Gel Based ZnO Nanorods Fabricated on Flexible Substrates. *Phys. Status Solidi RRL* **2013**, 7 (7), 493−496.

(12) Pérez-García, B.; Zúñiga-Pérez, J.; Muñoz-Sanjosé, V.; Colchero, J.; Palacios-Lidón, E. Formation and Rupture of Schottky Nanocontacts on ZnO Nanocolumns. *Nano Lett.* **2007**, 7 (6), 1505−1511.

(13) Qi, J.; Olmedo, M.; Zheng, J. G.; Liu, J. Multimode Resistive Switching in Single ZnO Nanoisland System. *Sci. Rep.* **2013**, 3, 2405.

(14) Gupta, M. K.; Kumar, B. High T_C Ferroelectricity in V-Doped ZnO Nanorods. *J. Mater. Chem.* **2011**, 21 (38), 14559−14562.

(15) Ghosh, M.; Rao, G. M. Interstitial Defects Induced Ferroelectricity in Undoped ZnO Nanorods at Room Temperature. *Sci. Adv. Mater.* **2013**, 5 (7), 733−739.

(16) Morozovska, A.; Eliseev, E.; Glinchuk, M. Ferroelectricity Enhancement in Confined Nanorods: Direct Variational Method. *Phys. Rev. B* **2006**, 73 (21), 214106.

(17) Scrymgeour, D. A.; Sounart, T. L.; Simmons, N. C.; Hsu, J. W. Polarity and Piezoelectric Response of Solution Grown Zinc Oxide Nanocrystals on Silver. *J. Appl. Phys.* **2007**, 101 (1), 014316.

(18) Kalinin, S. V.; Gruverman, A. *Scanning Probe Microscopy: Electrical and Electromechanical Phenomena at the Nanoscale*; Springer: New York, 2007; Vol. 1.

(19) Scrymgeour, D. A.; Hsu, J. W. P. Correlated Piezoelectric and Electrical Properties in Individual ZnO Nanorods. *Nano Lett.* **2008**, 8 (8), 2204−2209.

(20) Guo, M.; Diao, P.; Cai, S. Hydrothermal Growth of Well-Aligned ZnO Nanorod Arrays: Dependence of Morphology and Alignment Ordering Upon Preparing Conditions. *J. Solid State Chem.* **2005**, 178, 1864−1873.

(21) Kevin, M.; Tho, W. H.; Ho, G. W. Transferability of Solution Processed Epitaxial Ga:ZnO Films; Tailored for Gas Sensor and Transparent Conducting Oxide Applications. *J. Mater. Chem.* **2012**, 22 (32), 16442−16447.

(22) Kumar, A.; Herng, T. S.; Zeng, K.; Ding, J. Bipolar Charge Storage Characteristics in Copper and Cobalt Co-Doped Zinc Oxide (ZnO) Thin Film. *ACS Appl. Mater. Interfaces* **2012**, 4 (10), 5276−5280.

(23) Jain, V.; Kushto, G. P.; Wolak, M.; Mäkinen, A. J. Electrical Contact Fabrication on Vertically Aligned ZnO Nanowires Investigated by Current Sensing Afm. *Phys. Status Solidi A* **2013**, 210 (10), 2153−2158.

(24) Nadarajah, K.; Yern Chee, C.; Tan, C. Y. Influence of Annealing on Properties of Spray Deposited ZnO Thin Films. *J. Nanomater.* **2013**, 2013 (22), 1−8.

(25) Vayssieres, L.; Keis, K.; Lindquist, S.-E.; Hagfeldt, A. Purpose-Built Anisotropic Metal Oxide Material: 3d Highly Oriented Microrod Array of ZnO. *J. Phys. Chem. B* **2001**, 105 (17), 3350−3352.

(26) Xu, S.; Wang, Z. One-Dimensional ZnO Nanostructures: Solution Growth and Functional Properties. *Nano Res.* **2011**, 4 (11), 1013−1098.

(27) Ashfold, M. N.; Doherty, R. P.; Ndifor-Angwafor, N. G.; Riley, D. J.; Sun, Y. The Kinetics of the Hydrothermal Growth of ZnO Nanostructures. *Thin Solid Films* **2007**, 515 (24), 8679−8683.

(28) Richardson, J. J.; Lange, F. F. Controlling Low Temperature Aqueous Synthesis of ZnO. 1. Thermodynamic Analysis. *Cryst. Growth Des.* **2009**, 9 (6), 2570−2575.

(29) Richardson, J. J.; Lange, F. F. Controlling Low Temperature Aqueous Synthesis of ZnO. 2. A Novel Continuous Circulation Reactor. *Cryst. Growth Des.* **2009**, 9 (6), 2576−2581.

(30) Kong, Y. C.; Yu, D. P.; Zhang, B.; Fang, W.; Feng, S. Q. Ultraviolet-Emitting ZnO Nanowires Synthesized by a Physical Vapor Deposition Approach. *Appl. Phys. Lett.* **2001**, 78 (4), 407−409.

(31) Kang, H. S. Annealing Effect on the Property of Ultraviolet and Green Emissions of ZnO Thin Films. *J. Appl. Phys.* **2004**, 95 (3), 1246−1250.

(32) Wang, C.; Zhang, P.; Yue, J.; Zhang, Y.; Zheng, L. Effects of Annealing and Supersonic Treatment on the Structure and Photoluminescence of ZnO Films. *Phys. B (Amsterdam, Neth.)* **2008**, 403 (13−16), 2235−2240.

(33) Venkatesh, P. S.; Balakumar, S.; Jeganathan, K. Post-Annealing Effects on the Structural and Optical Properties of Vertically Aligned

Undoped ZnO Nanorods Grown by Radio Frequency Magnetron Sputtering. *RSC Adv.* **2014**, *4* (10), 5030−5035.

(34) Vanheusden, K.; Warren, W. L.; Seager, C. H.; Tallant, D. R.; Voigt, J. A.; Gnade, B. E. Mechanisms Behind Green Photoluminescence in ZnO Phosphor Powders. *J. Appl. Phys.* **1996**, *79* (10), 7983−7990.

(35) Greene, L. E.; Law, M.; Goldberger, J.; Kim, F.; Johnson, J. C.; Zhang, Y.; Saykally, R. J.; Yang, P. Low-Temperature Wafer-Scale Production of ZnO Nanowire Arrays. *Angew. Chem., Int. Ed.* **2003**, *42* (26), 3031−3034.

(36) Zhang, F.; Li, X.; Gao, X.; Wu, L.; Zhuge, F.; Wang, Q.; Liu, X.; Yang, R.; He, Y. Effect of Defect Content on the Unipolar Resistive Switching Characteristics of ZnO Thin Film Memory Devices. *Solid State Commun.* **2012**, *152* (17), 1630−1634.

(37) Lee, S.; Kim, H.; Park, J.; Yong, K. Coexistence of Unipolar and Bipolar Resistive Switching Characteristics in ZnO Thin Films. *J. Appl. Phys.* **2010**, *108* (7), 076101.

(38) Damjanovic, D. Ferroelectric, Dielectric and Piezoelectric Properties of Ferroelectric Thin Films and Ceramics. *Rep. Prog. Phys.* **1998**, *61* (9), 1280−1282.

(39) Kim, Y.; Bae, C.; Ryu, K.; Ko, H.; Kim, Y. K.; Hong, S.; Shin, H. Origin of Surface Potential Change During Ferroelectric Switching in Epitaxial $PbTiO_3$ Thin Films Studied by Scanning Force Microscopy. *Appl. Phys. Lett.* **2009**, *94* (3), 032907.

(40) Kalinin, S. V.; Rodriguez, B. J.; Jesse, S.; Karapetian, E.; Mirman, B.; Eliseev, E. A.; Morozovska, A. N. Nanoscale Electromechanics of Ferroelectric and Biological Systems: A New Dimension in Scanning Probe Microscopy. *Annu. Rev. Mater. Res.* **2007**, *37* (1), 189−238.

(41) Gao, P.; Nelson, C. T.; Jokisaari, J. R.; Baek, S. H.; Bark, C. W.; Zhang, Y.; Wang, E.; Schlom, D. G.; Eom, C. B.; Pan, X. Revealing the Role of Defects in Ferroelectric Switching with Atomic Resolution. *Nat. Commun.* **2011**, *2*, 591.

(42) Kalinin, S. V.; Morozovska, A. N.; Chen, L. Q.; Rodriguez, B. J. Local Polarization Dynamics in Ferroelectric Materials. *Rep. Prog. Phys.* **2010**, *73* (5), 056502.

(43) Bhattacharyya, S.; Saha, S. K.; Chakravorty, D. Silver Nanowires Grown in the Pores of a Silica Gel. *Appl. Phys. Lett.* **2000**, *77* (23), 3770−3772.

(44) Herng, T. S.; Kumar, A.; Ong, C. S.; Feng, Y. P.; Lu, Y. H.; Zeng, K. Y.; Ding, J. Investigation of the Non-Volatile Resistance Change in Noncentrosymmetric Compounds. *Sci. Rep.* **2012**, *2*, 587.

(45) Lee, M.-J.; Yoon, Y. S. Effect of Hydrogen Doping on Structural and Piezoelectric Properties of Sputtered ZnO Films. *Integr. Ferroelectr.* **2005**, *69* (1), 431−442.

(46) Van de Walle, C. G. Defect Analysis and Engineering in ZnO. *Phys. B (Amsterdam, Neth.)* **2001**, *308−310* (0), 899−903.

(47) Zhao, Q.; Xu, X. Y.; Song, X. F.; Zhang, X. Z.; Yu, D. P.; Li, C. P.; Guo, L. Enhanced Field Emission from ZnO Nanorods Via Thermal Annealing in Oxygen. *Appl. Phys. Lett.* **2006**, *88* (3), 033102.

(48) Park, C.; Chadi, D. Effect of Interstitial Hydrogen Impurities on Ferroelectric Polarization in $PbTiO_3$. *Phys. Rev. Lett.* **2000**, *84* (20), 4717.

(49) Stashans, A.; Chimborazo, J. Effect of Interstitial Hydrogen on Structural and Electronic Properties of $BaTiO_3$. *Philos. Mag. B* **2002**, *82* (10), 1145−1154.

(50) Rusop, M.; Uma, K.; Soga, T.; Jimbo, T. Post-Growth Annealing of Zinc Oxide Thin Films Pulsed Laser Deposited under Enhanced Oxygen Pressure on Quartz and Silicon Substrates. *Mater. Sci. Eng.: B* **2006**, *127* (2−3), 150−153.

(51) Sarkar, A.; Ghosh, S.; Chaudhuri, S.; Pal, A. Studies on Electron Transport Properties and the Burstein−Moss Shift in Indium-Doped ZnO Films. *Thin Solid Films* **1991**, *204* (2), 255−264.